

# Optically Switchable Fluorescence Enhancement at Critical Interparticle Distances

Arda Gulucu<sup>1</sup> and Emre Ozan Polat<sup>1,2,\*</sup>

<sup>1</sup>UNAM - Institute of Materials Science and Nanotechnology, Bilkent University, 06800, Ankara, Türkiye

<sup>2</sup>Department of Physics, Bilkent University, 06800, Ankara, Türkiye

Plasmonic nanostructures provide local field enhancement to be used as efficiency-boosting tools in fluorescence-based applications. For photostable quantum dots (QDs) to have enhanced emission, their size and exact location in the proximity of plasmonic nanostructure become key parameters while constructing light emitting devices. However, plasmonic nanostructures mostly suffer from non-radiative energy transfer at close proximity, which hinders the ultimate performance of fluorophores. In this work, we provided critical interparticle distances through finite difference time domain (FDTD) simulations, where the radiative decay rate is equalized to the non-radiative counterpart for light emitting QD-based technologies. To show the promises of the QD placement at a critical distance, we demonstrate an optical switch for the fluorescence efficiency of a CdSe/ZnS core-shell QD (CSQD) by optically exciting the silver nanoparticle (AgNP) placed at a critical distance. While the provided single particle spectroscopy allows for the observation of heterogeneity in CSQD-AgNP coupling that is often masked in ensemble measurements, our benchmark study serves as a base reference for the development of QD-based light emitting technologies by resolving the optically switchable active tuning of radiative decay rates.

## I. INTRODUCTION

Semiconducting QDs, particularly CdSe/ZnS CSQDs have gathered immense attention due to their size-tunable optical properties [1], high quantum yields and sustainable photostability [2]. Their size-dependent emission, a direct result of quantum confinement, allows for precise control over the emitted light's wavelength, making them invaluable in display technologies [3]. CdSe/ZnS CSQDs exhibit a broad absorption spectrum that extends from the UV to the visible region [4]. The absorption onset is size-dependent, with smaller QDs absorbing at shorter wavelengths (higher energy) and larger QDs absorbing at longer wavelengths (lower energy) [5]. The absorption spectrum typically shows multiple peaks corresponding to electronic transitions between quantized energy levels (i.e. 1S, 1P, 1D) [6]. On the other hand, the photoluminescence (PL) emission of CdSe/ZnS QDs is narrow and symmetric, with a full width at half maximum (FWHM) typically around 20 – 40 nm [7]. The emission wavelength is tunable by varying the core size, ranging from  $\sim 500$  nm (green) to  $\sim 650$  nm (red) for CdSe cores [8].

Superimposed on CdSe core, the ZnS shell plays a crucial role in passivating the CdSe core, significantly enhancing the quantum yield and photostability of these nanocrystals. ZnS capping results in high quantum yields (QYs) of up to 50 – 80 %, which is essential for long-duration applications like biological imaging [9] and QD displays [10]. While the development of QD-based sensors is rapidly advancing with applications ranging from environmental monitoring to medical diagnostics [11, 12], display side has majorly been commercialized providing ultra-high-definition resolutions [13].

In parallel, photonic research has seen a tremendous acceleration in plasmonics lately by the implementations of metal nanoparticles and metamaterials that are able to confine EM field in subwavelength scales [14]. However, looking at plasmonics from the device perspective, one can conclude that the plasmonic losses in metals due to non-radiative decay of plasmons strictly limits the application promises of using nanoplasmonic structures in technologically relevant device applications [15]. Although the compensation mechanisms have been demonstrated by using low loss/high gain materials, it remained as a technical difficulty to achieve full compensation [16].

AgNPs, with their strong localized surface plasmon resonances (LSPRs), offer a compelling platform for enhancing the fluorescence of nearby QDs [17]. The phenomenon of fluorescence enhancement arises from the interaction between the QD's excitonic transition and the AgNP's plasmonic field. This interaction can lead to an increase in the QD's radiative decay rate, resulting in brighter emission and shorter excited-state lifetimes [18]. However, probing the EM interactions to evaluate the degree of heterogeneity in QD-AgNP coupling on a single particle level is heavily restricted due to fluorescence blinking that majorly hinders the real-time particle tracking [19]. Moreover, experimental results on ensemble QD measurements report various absorption and scattering profiles due to the interference of multiple parameters such as size distribution, interaction with solvent and clustering effects [20].

To that end, in this article, we provide an FDTD study of a single CdSe/ZnS CSQD placed at various distances in the plasmonic hotspot region of AgNP. Our study reveals the EM interactions giving rise to radiative and non-radiative decay rates without being masked by externally interfering parameters. This allows us to locate the critical distances where the radiative decay is equalized to the non-radiative counterpart for each CSQD size and provides the determination of the CSQD-AgNP interpar-

\* Corresponding author: emre.polat@bilkent.edu.tr

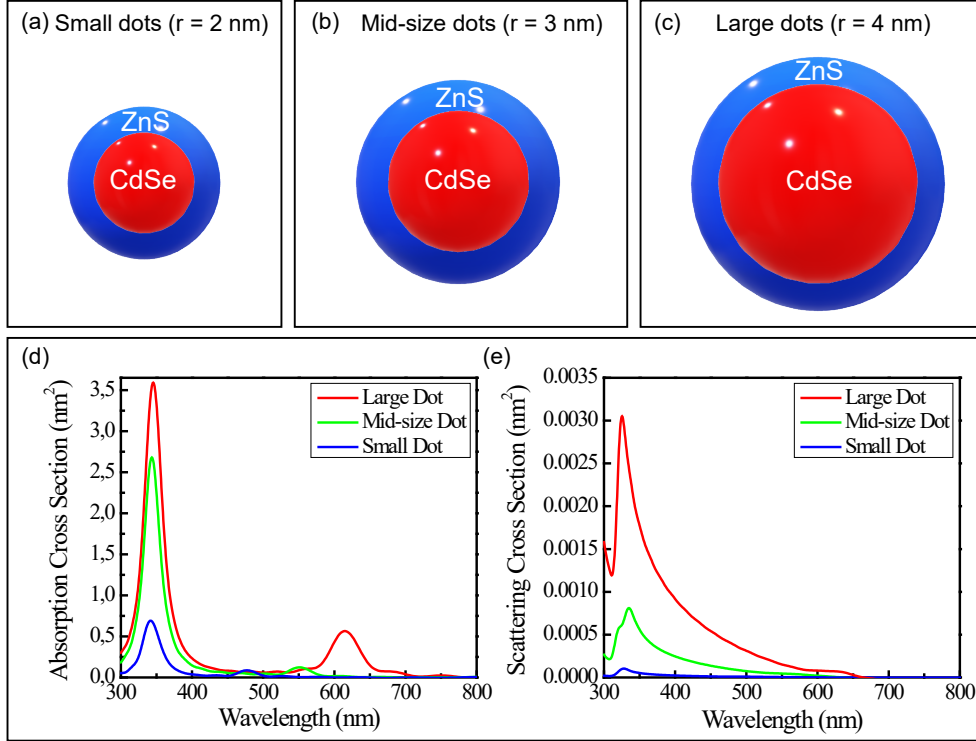


FIG. 1: (a) Schematic illustration of CdSe/ZnS CSQDs employed in the FDTD simulations as  $r = 2$  nm for the small dots, (b)  $r = 3$  nm for mid-size dots and (c)  $r = 4$  nm for the large dots. The core CdSe sizes are altered as  $r_{core} = 1$  nm, 2 nm and 3 nm while keeping the ZnS shell thickness constant as 1 nm. (d) Absorption cross section (ACS) spectra of large, mid-size and small dots under the irradiation of broadband EM wave (300 – 800 nm) with a peak position of 436 nm. (e) Scattering cross section (SCS) spectra of large mid-size and small dots under the same illumination conditions.

ticle distances leading to a measurable fluorescence enhancement solely due to the excitation of LSPR in AgNP. Although the literature has good number of FDTD plasmonic studies [21], this is the first time a fluorescence enhancement model of a particle system is reporting critical distances in Rayleigh limit where the particle size is much smaller than the incoming wavelength. The CSQDs are investigated as a complete model bridging their physical absorption and scattering cross section spectra to their dipole emission characteristics. Furthermore, to show the promises of working at the critical interparticle distances, we demonstrate an optically switchable fluorescence enhancement at a critical CSQD-AgNP interparticle distance for a proof-of-concept use in the QD-based light emitting applications.

## II. RESULTS

To provide a size classification of CSQDs that results in different EM wave interaction profiles, we employed three main CdSe core sizes without changing the ZnS shell size. Fig. 1 (a-c) shows the schematic illustration

of the employed CSQDs as small dots with radius  $r = 2$  nm (1 nm CdSe core + 1 nm ZnS shell), medium dots with radius  $r = 3$  nm (2 nm core CdSe core + 1 nm ZnS shell) and large dots with radius  $r = 4$  nm (3 nm CdSe core + 1 nm ZnS shell). Then, to investigate the EM interaction between an incoming EM wave and a single CSQD, we evaluated the absorption and scattering cross section spectra for the three sizes of single CdSe/ZnS CSQDs. We irradiate the CSQDs by a broadband EM wave of 300 - 800 nm plane wave pulse with a 436 nm peak position and 2 fs pulse length that is injected using total-field/scattered-field (TF/SF) method through Huygen's box source [22, 23]. Fig. 1 (d) shows the obtained absorption cross section (ACS) spectrum. Three-dimensional quantum confinement of charge carriers in CSQDs increases the effective band gap with decreasing CSQD size. Therefore, the optical absorption shifts to the lower wavelengths (higher energies) with decreasing CSQD size. The left-hand side dominating peak (Fig. 1 (d)) in the ultraviolet region demonstrates an enhanced absorption at higher energies (shorter wavelengths) due to the increasing surface coverage of ZnS shell. Since we employed the constant thickness of ZnS shell (1 nm)

TABLE I: Spectral parameters of the obtained absorption spectrum for different sizes of CdSe/ZnS CSQDs.

CSQD Radius nm	UV Peak Point, $\lambda_{UV}$ (ZnS Shell: 1 nm)	Visible Peak Point, $\lambda_{VIS}$ (CdSe-Core: 1,2,3 nm)	Peak Separation ( $\lambda_{UV} - \lambda_{VIS}$ )	FWHM (UV)	FWHM (VIS)
2	345.5 nm	615.0 nm	269.5 nm	29.9 nm	49.4 nm
3	343.6 nm	551.3 nm	207.7 nm	31.1 nm	39.6 nm
4	341.8 nm	477.1 nm	135.3 nm	30.1 nm	32.1 nm

for increasing core CdSe radius, the resulting UV absorption peak does not exhibit any energy shift. On the other hand, we observe a stark red shift in longer wavelength absorption peak that is associated to the increasing CdSe core radius. The resulting spectral parameters such as peak points, separation bandwidth and full width at half maximum (FWHM) values are given in Table I. Due to the tunable peak separation bandwidth, we emphasize that using the constant-shell-varying-core approach allows controllable band selection (rejection) for the photodiodes using CSQDs. To further investigate the EM interaction between the incoming irradiation and varying size CdSe/ZnS CSQDs, we obtained scattering cross section (SCS) spectrum.

Fig. 1 (e) shows SCS spectrum under the same broadband irradiation used for identifying the ACS spectrum. The profile of the SCS spectrum plays an important role in identifying the nature and efficiency of different scattering types such as Rayleigh, Mie and Raman scattering. For the employed CSQDs (with radius smaller than 10 nm) the dominant scattering type is Rayleigh scattering since the particle size is much smaller than the incident wavelength. In Rayleigh scattering, the intensity is proportional to the sixth power of the particle radius while it is inversely proportional to the fourth power of the incident wavelength ( $\sigma_s \sim R^6/\lambda^4$ ). Therefore, the SCS spectrum in Fig. 1 (e) shows a dominating UV and blue light scatter compared to rest of the visible spectrum while the particle size increases the scattering abruptly due to the sixth power dependence. Together with the ACS given in Fig. 1 (d), the SCS gives the profile of the total extinction that quantifies the resulting energy loss of the incident EM wave, which presents a key enabling mechanism to identify the nature of light-matter interactions.

Based on the obtained ACS and SCS profiles, we investigated the emission spectrum of different sized CSQDs. Due to the Stokes shift, the emission peaks redshift compared to the absorption peaks [24]. By adding Stokes shift values of  $\Delta\lambda = 15.4, 17$  and  $17.7$  nm for large, mid-size and small CSQDs respectively in conjunction with the experimental data [25], we obtained the emission intensity of the CdSe/ZnS CSQDs as dipole sources in our FDTD simulation (Fig. 2 (a)). Size dependent dipole emission spectra is provided by assigning Lorentzian distributions with peak points at 494.8, 568.3 and 630.4 nm and full width at half maximum (FWHM) linewidths of 27.4, 33.2 and 35.6 nm in compliance with the previous experimental data [5, 26, 27]. It is worth not-

ing that the resulting spectral width is narrower due to the excitation from the lowest energy state and quantum yield variations are omitted to be able to provide a consistent model. Next, we studied a single particle model that the CdSe/ZnS CSQD is placed in a proximity to spherical AgNP to reveal and use the interparticle EM interactions giving rise to fluorescence enhancement. Fig. 2 (b) shows the schematic illustration of the system of materials and their corresponding positioning in free space. We employed a spherical AgNP with a radius of 10 nm around which the EM field is strongly enhanced due to LSPR. Typically, for visible to near-infrared (400 – 800 nm) excitation, this hotspot region extends from the surface of AgNP up to 20 nm. To that end, we investigated the distance dependence of radiative and non-radiative decay rates in the hotspot region (2 – 20 nm). Fig. 2 (c-e) show the distance dependence of radiative and non-radiative decay rates for increasing CSQD radius respectively. In our free space FDTD simulations, we observed that, at short distances, energy is mostly transferred non-radiatively from the CSQD to the AgNP. Since plasmons decay non-radiatively, this behaviour at short interparticle distances is often related to dissipation in which the energy from plasmon excitation is converted into heat via electron-phonon and phonon-phonon interactions. This process includes Förster Resonant Energy Transfer (FRET) mechanism between the dipole source of CdSe/ZnS fluorescent CSQD as a donor and the spherical AgNP as an acceptor. FRET efficiency is strictly related to the spectral overlap between the donor and the acceptor. In our case, the emission peaks and Lorentzian distribution around them spectrally overlaps with AgNP's peak around 400 - 450 nm. For larger CSQDs that emit around 630 nm, the spectral overlap is less which causes a lower FRET efficiency. As shown in the decay rate plots (Fig. 2 (c-e)), with the increment of CSQD-AgNP interparticle distance, the CSQD's radiative decay rate starts to overcome the nonradiative decay rate by Purcell factor enhancement boosting the fluorescence emission. As detailed above, FRET quenching dominates at very close separations while the radiative benefits are outstripping at intermediate separations. This is due to the off-resonance configuration in which there is no complete overlap between AgNP and CdSe/ZnS spectra yielding CSQDs with modest fluorescence enhancement. Even under this off-resonance condition, the enhanced local EM field produced by the AgNP can induce fluorescence enhancement by increasing the excitation rate. This interplay between non-radiative

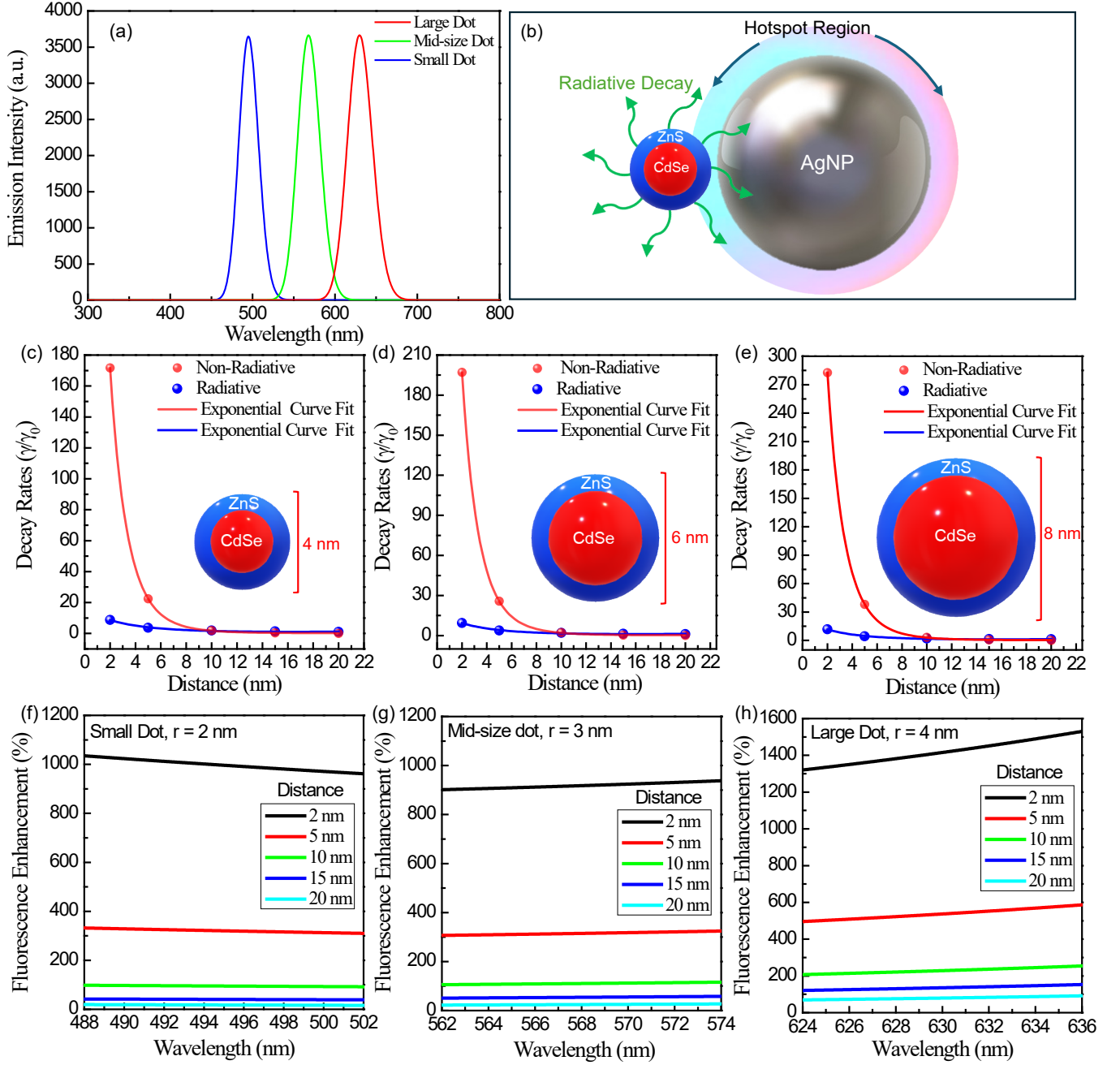


FIG. 2: (a) Emission spectra for each size of CdSe/ZnS CSQDs modelled using the corresponding Stokes shifts on the ACS spectra. (b) Schematic illustration of the free-space modelled system of a single fluorescent CdSe/ZnS CSQD placed in the hotspot region of AgNP. (c) Nonradiative and radiative decay rates of CdSe/ZnS CSQDs with respect to the distance from the AgNP surface for a CSQD radius of  $r = 2$  nm (small dots), (d) for mid-size dots with  $r = 3$  nm and (e) for large dots with  $r = 4$  nm. Exponential curve fit in the form of  $e^{a+bx+cx^2}$  is applied to define the critical distances as 12.18 nm 10.73 nm and 10.36 nm for small, mid-size and large dot size respectively. (f) Fluorescence enhancement spectra within the emission linewidth of small dots, (g) mid-size dots and (h) large dots with respect to distance from the AgNP surface.



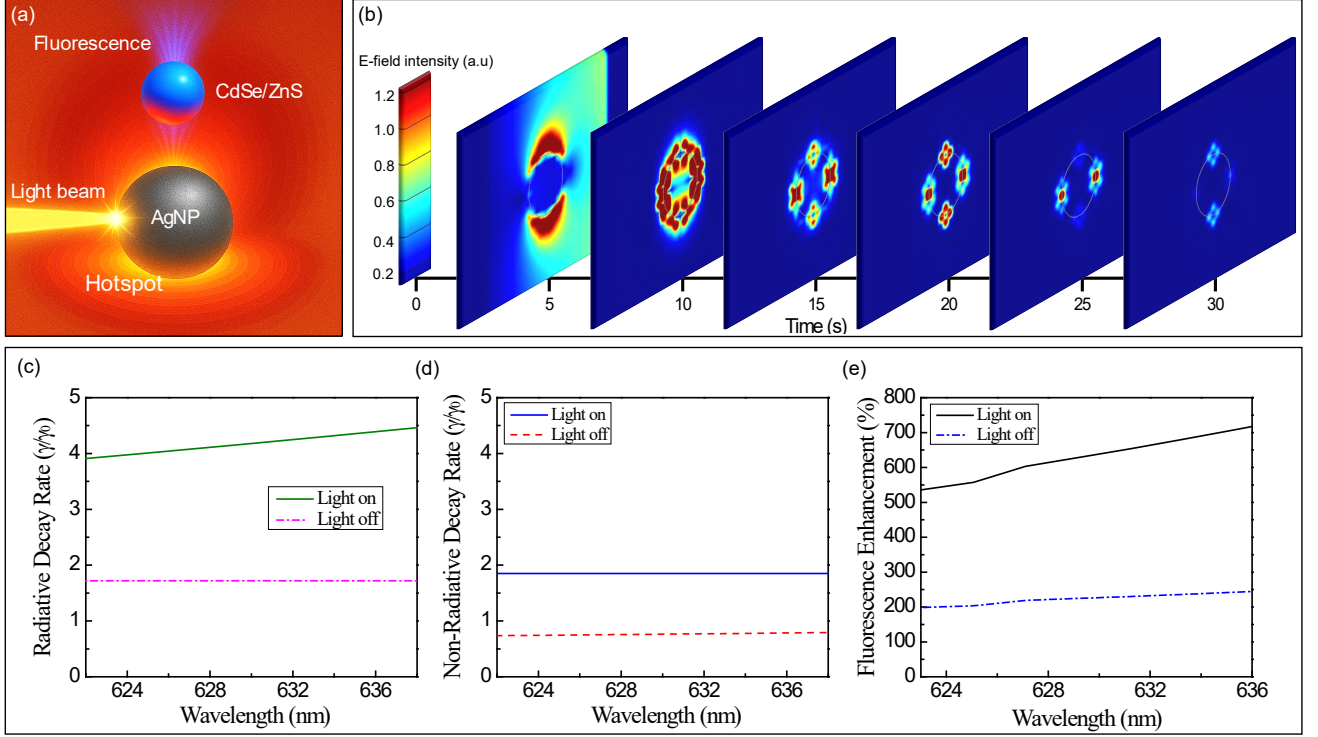


FIG. 3: (a) Schematic illustration of the optical excitation of AgNP and the resulting fluorescence enhancement from CdSe/ZnS. (b) Temporal response showing the E-Field intensity localization on AgNP surface under the injected broadband plane wave pulse (300 – 800 nm). (c) Recorded radiative decay rate from the dipole emission of CdSe/ZnS CSQD with and without light pulse injection to AgNP surface. (d) Recorded non-radiative decay rate under the same illumination conditions. (e) Fluorescence enhancement spectrum showing the optically switchable enhancement behaviour reaching up to an observable 720 % enhancement within the emission bandwidth of the CSQD.

FRET mechanism and the near field enhancement that boosts the Purcell factor is mainly responsible for the determination of the obtained critical distance values when the system is off resonance [28, 29]. In that sense, the critical CSQD-AgNP interparticle distance where the radiative decay is equalized the non-radiative counterpart for each dot size is obtained from the FDTD simulations by applying a curve fit to the decay rate spectral data as shown in Fig. 2 (c-e). The applied exponential is in the form  $e^{a+bx+cx^2}$  providing the critical distance values as 10.36, 10.73 and 12.18 nm for large, mid-size and small dots, respectively with a standard error of  $\pm 7 \times 10^{-6}$  nm for the small and  $\pm 0.18$  nm for the mid-size and large dot size. More interestingly, after the radiative decay is equalized to the non-radiative decay at the critical point, both rates kept decreasing while the non-radiative rate diminishes faster; increasing the difference between the rates that reaches up to 0.96 for the large, 1.06 for the mid-size and 1.07 for the small dot size. To show the results of radiative decay rate enhancement in the presence of AgNP, we plotted the percentage fluorescence enhancement with respect to various interparticle distances in Fig. 2 (f-h).

Due to the hotspot region around the AgNP, where the strong local EM field enhancement occurs, excitation rate of nearby fluorophores are enhanced creating higher probability of photon absorption. This leads to more emission events as the fluorescence intensity increases. By comparing the original emission spectra with the boosted radiative decay rate near the AgNP, we created the percentage fluorescence enhancement spectra within the emission bandwidths of three different dot sizes. While the large dot shows profound increment in the enhancement with respect to wavelength, we observed that the effect is less pronounced in the mid-size dots and diminishing for the small-size CSQDs yielding a constant enhancement within the bandwidth. It is clear from the plots that by deterministically placing CdSe/ZnS CSQDs within the hotspot region of the AgNP (2 - 20 nm) one can boost the fluorescence three orders of magnitude. Both the size confinement and the proximity to AgNP have positive contribution to the fluorescence enhancement, however this behaviour is given independently from the non-radiative decay rates that are shown in Fig. 2 (c-e) which dominates at closer dis-

tances and suppress the fluorescence for the external observer. This itself emphasizes the importance of working in the critical interparticle distances to benefit from the LSPR enhancement in the absence of gain mechanisms. To further demonstrate the promises of the working at critical interparticle distances, we demonstrate an optically switchable dipole emission of large CdSe/ZnS CSQD ( $r = 4$  nm) at the critical distance (10.36 nm) from the excited AgNP by incoming irradiation. By irradiating AgNP via collimated light beam shined on the surface (Fig. 3 (a)), we recorded the effects of the boosted hotspot region on the fluorescence enhancement. Fig. 3 (a) shows the schematic illustration of the experiment simulation. To solely resolve and investigate the effect of the LSPR enhancement on the fluorescence intensity, a broadband (300 - 800 nm) EM wave pulse is sent to the AgNP surface without any direct contribution to the initial photoluminescence of CdSe/ZnS either from the light source itself or the scattering from the surface. The temporal E-field intensity localization and the resulting LSPR oscillations forming the hotspot regions is shown in Fig. 3 (b).

The recorded radiative and non-radiative dipole emission from the CdSe/ZnS CSQDs under the light excitation of AgNP are shown in Fig. 3 (c) and (d). The effect of light-matter interaction causing enhanced field localization in AgNP shows itself as a boost in both radiative (Fig. 3 (c)) and non-radiative (Fig. 3 (d)) decay rates. However, working in the critical distance allows the radiative decay rate enhancement to become more pronounced (Fig. 3 (c)) and not suppressed by the non-radiative counterpart (Fig. 3 (d)). This creates an additional optically switchable fluorescence enhancement to the initial passive enhancement due to spatial proximity of the particles (Fig. 3 (e)). According to our model, one can achieve an observable 720 % fluorescence enhancement solely from the increase in the AgNP excitation with the light application. In practical applications however, scattering from the AgNP surface will further enhance the measured intensity and using a larger light spot size can also provide direct contribution to this, which are different from the original fluorescent enhancement solely due to the AgNP excitation. Thus, these effects are excluded from our simulations by monitoring the scattered (or directed) light intensity reaching out to power monitors that counts the radiative and non-radiative decay rate of the original dipole emission. The simulation can be repeated for various environmental dielectric constants to extract the critical distances within the target device substrate or the QD synthesis media including liquid dispersions.

### III. CONCLUSION AND DISCUSSION

After Yee's algorithm to shift electric and magnetic fields in discretized space and time for the solution of Maxwell's equations [30], FDTD method has been

applied to many plasmonic and photonic systems with the advancement of computer technology that allows for the discretization of space in sub-wavelength dimensions [21]. Pure analytical methods fall short in calculating the near fields in complex scenarios, therefore, here we implement an FDTD simulation with Yee cell (mesh) size that is much smaller (1.4 nm) than the incident wavelength (300 - 800nm) that can overcome complex nanostructures with superimposed materials such as CdSe/ZnS CSQDs. By precisely changing the interparticle distance between individual CSQD and AgNP for each CSQD size, we elucidate the EM interactions giving rise to fluorescence enhancement, FRET and non-radiative decay. Our FDTD model provides for the first time critical QD-AgNP interpar by simultaneously measuring the radiative and non-radiative decay rates. We extracted the critical distance points where the suppression of radiative decay is no longer effective, yielding observable fluorescence enhancement in the absence of any gain mechanism. This behavior underscores a central principle in plasmon-enhanced fluorescence: maximal brightness is achieved not simply by maximizing the coupling strength, but by balancing radiative enhancement against nonradiative quenching. Our findings are consistent with theoretical models and previous experimental studies which have demonstrated that the highest fluorescence enhancements are observed in systems where the emitter is optimally detuned or positioned to favor radiative decay over nonradiative losses [31].

The implementation of critical distances found in our simulations are demonstrated as an optically switchable fluorescence enhancement in which the AgNP is exposed to broadband illumination. By increasing the local field enhancement on AgNP, we provided an active optical fluorescence intensity control scheme for the large dot ( $r = 4$  nm) yielding up to 720 % enhancement without being suppressed by non-radiative decay mechanism. Our model can be generalized to find critical distances and the amount of enhancement for the fluorescent materials with known refractive index data in the Rayleigh limit where the size properties are much smaller than the wavelength ( $d \ll \lambda$ ). Since the heterogeneity in CSQD-AgNP coupling is often masked in ensemble measurements, we anticipate that our study serves as a benchmark for the development of QD-based light emitting technologies using fluorescence enhancement. Similarly, the provided size dependent ACS and SCS spectra can be implemented in photodetection technologies using the size and positioning of QDs as an active parameter in the absorber layers. Our free space model can be adapted to other media by changing the environmental dielectric constant, which allows to determine the critical distances for the device structures or liquid phase dispersions that contain small fluorescent particles.

#### IV. METHODOLOGY

We simulate the optical behavior of CdSe-ZnS CSQDs in free space with and without the presence of closely located AgNP using FDTD technique to solve Maxwell's equations. Maxwell's curl equations are discretized in both time and space:

$$\nabla \times \mathbf{E} = -\mu \frac{\partial \mathbf{H}}{\partial t}, \quad (1)$$

$$\nabla \times \mathbf{H} = \epsilon \frac{\partial \mathbf{E}}{\partial t} + \mathbf{J}, \quad (2)$$

where  $\mathbf{E}$  and  $\mathbf{H}$  are electric and magnetic fields,  $\mu$  is the permeability,  $\epsilon$  is the permittivity and  $\mathbf{J}$  is the current density. FDTD enables the simulation of complex interactions between the quantum dot and the plasmonic nanoparticle, capturing both near-field enhancements and far-field scattering/absorption effects. To simulate an open, infinite field and reduce spurious reflections from the field boundaries, a Perfectly Matched Layer (PML) was implemented in FDTD simulations. The free space model is implemented in 3D FDTD solver (Lumerical, FDTD solutions). The PML was configured to absorb outgoing waves with minimal reflection by gradually increasing the electrical conductivity in the absorber region. This caused the electromagnetic fields to decay exponentially as they approached the boundaries, effectively simulating an infinite field.

To calculate the absorption and scattering cross sections of the CSQDs, the light source (TF/SF) source was emitted from the interior of the PML in the form of a plane wave packet at broadband spectrum mostly covering the visible region (300 – 800 nm). To guarantee numerical stability, the simulation space is discretized in both space and time using the Courant condition. With a constant ZnS shell thickness of 1 nm, three CdSe/ZnS CSQDs with radii 2 nm, 3 nm, and 4 nm are evaluated.

A frequency dependent Lorentzian dielectric function is used for the core and shell materials of the varying size CSQDs with corresponding parameters to characterize the light-matter interaction and the resulting optical response;

$$\epsilon(\omega) = \epsilon_{\infty} + \frac{f \omega_0^2}{\omega_0^2 - \omega^2 - i \gamma \omega},$$

where,  $\epsilon_{\infty}$  is the background dielectric constant,  $f$  is the oscillator strength quantifying the transition strength,  $\omega_0$  is the resonance (or natural) frequency corresponding to the electronic transition,  $\omega$  is the angular frequency of the incident electromagnetic field,  $\gamma$  is the damping constant representing losses, and the imaginary unit indicating the phase shift between the driving field and the polarization response. The large CSQD has a linewidth of  $\sim 10^{14}$  Hz to simulate a lossy environment, a core Lorentz oscillator strength of 0.15, and a background permittivity of 5.6. The ZnS shell is modeled

with a background permittivity of 5.2 and a Lorentzian contribution of 0.5. The overall optical response of each CSQD is obtained by combining the dielectric functions. The ACS and SCS spectra are extracted as:

$$\sigma_{\text{abs}}(\omega) = \frac{\omega}{c \epsilon_0} \text{Im}[\alpha(\omega)], \quad \sigma_{\text{sca}}(\omega) = \frac{k^4}{6\pi} \text{Re}[\alpha(\omega)]. \quad (3)$$

where  $k = \omega/c$  is the wavenumber,  $\alpha(\omega)$  is the polarizability of the dot,  $c$  is the speed of light and  $\epsilon_0$  is the permittivity of the free space. Radiative and non-radiative decay rates as function of CSQD-AgNP interparticle spacing are calculated to assess the decay dynamics. CdSe/ZnS CSQDs are modelled as dipole sources emitting at the corresponding emission frequencies (absorption wavelength + Stokes shift). Their decay rate in free space is expressed as

$$\gamma_0 = \frac{\omega^3 |p|^2}{3\pi \epsilon_0 \hbar c^3}, \quad (4)$$

where,  $\omega$  is the angular frequency,  $|p|$  is the dipole moment,  $\epsilon_0$  is the vacuum permittivity,  $\hbar$  is the Planck's constant, and  $c$  is the speed of light. To isolate the energy that is emitted as light (radiated power) in the presence of AgNP, we use far-field power monitors. The radiative decay rate is

$$\gamma_{\text{rad}} = \frac{P_{\text{rad}}}{P_0} \gamma_0, \quad (5)$$

where  $P_{\text{rad}}$  is the power measured by monitors in the far-field. Total decay rate is then

$$\gamma_{\text{tot}} = \frac{P_{\text{tot}}}{P_0} \gamma_0, \quad (6)$$

where  $P_{\text{tot}}$  is the power measured by monitors in the near field. And the non-radiative decay rate is,

$$\gamma_{\text{nonrad}} = \gamma_{\text{tot}} - \gamma_{\text{rad}}. \quad (7)$$

Near-field power monitors positioned to cover emitting dipole and AgNP respectively to capture all energy flows, including those modified by the antenna's near-field coupling, which is

$$P_{\text{tot}} = \oint_s \mathbf{S} \cdot d\mathbf{A}, \quad (8)$$

where  $\mathbf{S}$  is the Poynting vector. Analogously,

$$P_{\text{rad}} = \oint_{s_{\text{far}}} \mathbf{S} \cdot d\mathbf{A}, \quad (9)$$

is the power calculated by far-field monitors of a chosen surface (simulation domain) such that non-radiative losses are not captured, isolating the radiative decay enhanced by LSPR. The distance dependence of these rates

is quantified by application of exponential curve fit. Standard Error in the critical distances are calculated from the applied exponent in the form:

$$y_i(x) = \exp(a_i + b_i x + c_i x^2), \quad i = 1, 2, \quad (10)$$

where the coefficients  $a_i$ ,  $b_i$  and  $c_i$  are obtained from independent fits. The critical (or intersection) point  $x^*$  is defined by the condition

$$y_1(x^*) = y_2(x^*). \quad (11)$$

Defining a difference function at the intersection,

$$F(x) = y_1(x) - y_2(x), \quad \text{with } F(x^*) = 0. \quad (12)$$

We assume that near the critical point the measured  $y$ -values are subject to a typical uncertainty  $\delta y$ . If the uncertainties for  $y_1$  and  $y_2$  are approximately equal and independent, the uncertainty in the difference is given by

$$\delta F \approx \sqrt{(\delta y_1)^2 + (\delta y_2)^2} \approx \sqrt{2} \delta y. \quad (13)$$

Expanding  $F(x)$  in a first-order Taylor series about  $x^*$ :

$$F(x^* + \delta x) \approx F(x^*) + F'(x^*) \delta x. \quad (14)$$

At the the intersection point

$$\delta F \approx F'(x^*) \delta x. \quad (15)$$

Rearranging,

$$\delta x \approx \frac{\delta F}{|F'(x^*)|} \approx \frac{\sqrt{2} \delta y}{|F'(x^*)|}, \quad (16)$$

where  $F'(x^*)$  is the derivative of the difference function at  $x = x^*$ . To compute  $F'(x^*)$ , note that each curve is given by  $y_i(x) = \exp(a_i + b_i x + c_i x^2)$  and its derivative

with respect to  $x$  is  $y'_i(x) = y_i(x)(b_i + c_i x)$ . Thus, the derivative of the difference function is

$$F'(x^*) = y'_1(x^*) - y'_2(x^*)$$

$$= y_1(x^*)(b_1 + c_1 x^*) - y_2(x^*)(b_2 + c_2 x^*).$$

Evaluating this derivative at the critical point,  $x = x^*$ , the uncertainty in critical distances are found using:

$$\delta x \approx \frac{\sqrt{2} \delta y}{|y_1(x^*)(b_1 + c_1 x^*) - y_2(x^*)(b_2 + c_2 x^*)|}. \quad (17)$$

## V. ACKNOWLEDGEMENTS

E.O.P acknowledges the support from TUBITAK (222N308, CHIST-ERA) and Bilkent University-TUBITAK BILGEM Consultancy Call for Research Proposals for the 2024-2025 academic year.

## VI. AUTHOR CONTRIBUTIONS

A.G ran the simulations, performed the calculations and extracted the the raw data forming the basis of the shown results and contributed to the formation of the manuscript. E.O.P conceptualized and supervised the idea and majorly contributed to the formation of the manuscript.

## VII. COMPETING INTERESTS

The authors declare no competing interests.

## VIII. DATA AVAILABILITY

All the data needed to evaluate the shown results is present within the paper. Additional data related to the paper that support the findings of this study are available from the corresponding author upon reasonable requests.

- 
- [1] Peng, X.; Manna, L.; Yang, W.; Wickham, J.; Scher, E.; Kadavanich, A.; Alivisatos, A. P. Shape control of CdSe nanocrystals. *Nature* **2000**, *404*, 59–61.
  - [2] Fu, Y.; Kim, D.; Jiang, W.; Yin, W.; Ahn, T. K.; Chae, H. Excellent stability of thicker shell CdSe@ZnS/ZnS quantum dots. *RSC advances* **2017**, *7*, 40866–40872.
  - [3] Colvin, V.; Schlamp, M.; Alivisatos, A. Light-emitting diodes made from cadmium selenide nanocrystals and a semiconducting polymer. *SPIE milestone series* **2005**, *180*, 396–398.
  - [4] Dabbousi, B. O.; Rodriguez-Viejo, J.; Mikulec, F. V.; Heine, J. R.; Mattoussi, H.; Ober, R.; Jensen, K. F.; Bawendi, M. G. (CdSe) ZnS core-shell quantum dots: synthesis and characterization of a size series of highly luminescent nanocrystallites. *The Journal of Physical Chemistry B* **1997**, *101*, 9463–9475.
  - [5] Jasieniak, J.; Smith, L.; Van Embden, J.; Mulvaney, P.; Califano, M. Re-examination of the size-dependent absorption properties of CdSe quantum dots. *The Journal of Physical Chemistry C* **2009**, *113*, 19468–19474.

- [6] Alivisatos, A. P. Semiconductor clusters, nanocrystals, and quantum dots. *science* **1996**, *271*, 933–937.
- [7] Ibaouf, K.; Prasad, S.; Hamdan, A.; Alsalmi, M.; Aldwayyan, A.; Zaman, M.; Masilamani, V. Photoluminescence spectra of CdSe/ZnS quantum dots in solution. *Spectrochimica acta part A: Molecular and biomolecular spectroscopy* **2014**, *121*, 339–345.
- [8] Polovitsyn, A.; Dang, Z.; Movilla, J. L.; Martín-García, B.; Khan, A. H.; Bertrand, G. H.; Brescia, R.; Moreels, I. Synthesis of air-stable CdSe/ZnS core-shell nanoplatelets with tunable emission wavelength. *Chemistry of Materials* **2017**, *29*, 5671–5680.
- [9] Medintz, I. L.; Uyeda, H. T.; Goldman, E. R.; Mattoussi, H. Quantum dot bioconjugates for imaging, labelling and sensing. *Nature materials* **2005**, *4*, 435–446.
- [10] Huang, Y.-M.; Singh, K. J.; Liu, A.-C.; Lin, C.-C.; Chen, Z.; Wang, K.; Lin, Y.; Liu, Z.; Wu, T.; Kuo, H.-C. Advances in quantum-dot-based displays. *Nanomaterials* **2020**, *10*, 1327.
- [11] Rana, M.; Chowdhury, P. L-glutathione capped CdSe/ZnS quantum dot sensor for the detection of environmentally hazardous metal ions. *Journal of Luminescence* **2019**, *206*, 105–112.
- [12] Azzazy, H. M.; Mansour, M. M.; Kazmierczak, S. C. From diagnostics to therapy: prospects of quantum dots. *Clinical biochemistry* **2007**, *40*, 917–927.
- [13] Dai, X.; Deng, Y.; Peng, X.; Jin, Y. Quantum-dot light-emitting diodes for large-area displays: towards the dawn of commercialization. *Advanced materials* **2017**, *29*, 1607022.
- [14] Khurgin, J. B. How to deal with the loss in plasmonics and metamaterials. *Nature nanotechnology* **2015**, *10*, 2–6.
- [15] Khurgin, J. B.; Sun, G. Scaling of losses with size and wavelength in nanoplasmonics and metamaterials. *Applied Physics Letters* **2011**, *99*.
- [16] Khurgin, J. B.; Boltasseva, A. Reflecting upon the losses in plasmonics and metamaterials. *MRS bulletin* **2012**, *37*, 768–779.
- [17] Kelly, K. L.; Coronado, E.; Zhao, L. L.; Schatz, G. C. The optical properties of metal nanoparticles: the influence of size, shape, and dielectric environment. 2003.
- [18] Novotny, L.; Van Hulst, N. Antennas for light. *Nature photonics* **2011**, *5*, 83–90.
- [19] Qin, H.-Y.; Shang, X.-J.; Ning, Z.-J.; Fu, T.; Niu, Z.-C.; Brismar, H.; Ågren, H.; Fu, Y. Observation of bunched blinking from individual CdSe/CdS and CdSe/ZnS colloidal quantum dots. *The Journal of Physical Chemistry C* **2012**, *116*, 12786–12790.
- [20] Leatherdale, C. A.; Woo, W.-K.; Mikulec, F. V.; Bawendi, M. G. On the absorption cross section of CdSe nanocrystal quantum dots. *The Journal of Physical Chemistry B* **2002**, *106*, 7619–7622.
- [21] Lesina, A. C.; Vaccari, A.; Berini, P.; Ramunno, L. On the convergence and accuracy of the FDTD method for nanoplasmonics. *Optics Express* **2015**, *23*, 10481–10497.
- [22] Umashankar, K.; Taflov, A. A novel method to analyze electromagnetic scattering of complex objects. *IEEE transactions on electromagnetic compatibility* **1982**, 397–405.
- [23] Merewether, D.; Fisher, R.; Smith, F. On implementing a numeric Huygen’s source scheme in a finite difference program to illuminate scattering bodies. *IEEE Transactions on Nuclear Science* **1980**, *27*, 1829–1833.
- [24] Bagga, A.; Chattopadhyay, P.; Ghosh, S. Origin of Stokes shift in InAs and CdSe quantum dots: Exchange splitting of excitonic states. *Physical Review B—Condensed Matter and Materials Physics* **2006**, *74*, 035341.
- [25] Karim, M. R.; Balaban, M.; Ünlü, H. Strain effects on the band gap and diameter of CdSe core and CdSe/ZnS core/shell quantum dots at any temperature. *Advances in Materials Science and Engineering* **2019**, *2019*, 3764395.
- [26] Talapin, D. V.; Rogach, A. L.; Kornowski, A.; Haase, M.; Weller, H. Highly luminescent monodisperse CdSe and CdSe/ZnS nanocrystals synthesized in a hexadecylamine-trioctylphosphine oxide-trioctylphosphine mixture. *Nano letters* **2001**, *1*, 207–211.
- [27] Peng, X.; Schlamp, M. C.; Kadavanich, A. V.; Alivisatos, A. P. Epitaxial growth of highly luminescent CdSe/CdS core/shell nanocrystals with photostability and electronic accessibility. *Journal of the American Chemical Society* **1997**, *119*, 7019–7029.
- [28] Willets, K. A.; Van Duyne, R. P. Localized surface plasmon resonance spectroscopy and sensing. *Annu. Rev. Phys. Chem.* **2007**, *58*, 267–297.
- [29] Lakowicz, J. R. *Principles of fluorescence spectroscopy*; Springer, 2006.
- [30] Yee, K. Numerical solution of initial boundary value problems involving Maxwell’s equations in isotropic media. *IEEE Transactions on antennas and propagation* **1966**, *14*, 302–307.
- [31] Anger, P.; Bharadwaj, P.; Novotny, L. Enhancement and quenching of single-molecule fluorescence. *Physical review letters* **2006**, *96*, 113002.